Materials Science & Engineering C 122 (2021) 111933

Contents lists available at ScienceDirect

Materials Science & Engineering C

journal homepage: www.elsevier.com/locate/msec

Pore geometry influences growth and cell adhesion of infrapatellar mesenchymal stem cells in biofabricated 3D thermoplastic scaffolds useful for cartilage tissue engineering

D. Martínez-Moreno [a,b,c,d], G. Jiménez [a,b,c,d], C. Chocarro-Wrona [a,b,c,d], E. Carrillo [a,b,c,d], E. Montañez [e], C. Galocha-León [f], B. Clares-Naveros [f], P. Gálvez-Martín [f,g], G. Rus [d,h], J. de Vicente [d,i,*], J.A. Marchal [a,b,c,d,**]

[a] Instituto de Investigación Biosanitaria de Granada (ibs.GRANADA), University Hospitals of Granada-University of Granada, Granada, Spain
[b] Biopathology and Regenerative Medicine Institute (IBIMER), Centre for Biomedical Research (CIBM), University of Granada, Granada, Spain
[c] Department of Human Anatomy and Embryology, Faculty of Medicine, University of Granada, Granada, Spain
[d] Excellence Research Unit "Modeling Nature" (MNat), University of Granada, Granada, Spain
[e] Department of Orthopedic Surgery and Traumatology, Virgen de la Victoria University Hospital, 29010 Málaga, Spain
[f] Department of Pharmacy and Pharmaceutical Technology, Faculty of Pharmacy, University of Granada, Granada, Spain
[g] R&D Human Health, Bioibérica S.A.U., Barcelona E-08029, Spain
[h] Department of Structural Mechanics, University of Granada, Politécnico de Fuentenueva, Granada E-18071, Spain
[i] Department of Applied Physics, Faculty of Sciences, University of Granada, Granada, Spain

ARTICLE INFO

Keywords:
Cartilage tissue engineering
Polycaprolactone
1,4-Butanediol thermoplastic polyurethane
Rheology
Microstructure
Porosity
Infrapatellar mesenchymal stem cells

ABSTRACT

The most pressing need in cartilage tissue engineering (CTE) is the creation of a biomaterial capable to tailor the complex extracellular matrix of the tissue. Despite the standardized used of polycaprolactone (PCL) for osteochondral scaffolds, the pronounced stiffness mismatch between PCL scaffold and the tissue it replaces remarks the biomechanical incompatibility as main limitation. To overcome it, the present work was focused in the design and analysis of several geometries and pore sizes and how they affect cell adhesion and proliferation of infrapatellar fat pad-derived mesenchymal stem cells (IPFP-MSCs) loaded in biofabricated 3D thermoplastic scaffolds. A novel biomaterial for CTE, the 1,4-butanediol thermoplastic polyurethane (b-TPUe) together PCL were studied to compare their mechanical properties. Three different geometrical patterns were included: hexagonal (H), square (S), and, triangular (T); each one was printed with three different pore sizes (PS): 1, 1.5 and 2 mm. Results showed differences in cell adhesion, cell proliferation and mechanical properties depending on the geometry, porosity and type of biomaterial used. Finally, the microstructure of the two optimal geometries (T1.5 and T2) was deeply analyzed using multiaxial mechanical tests, with and without perimeters, μCT for microstructure analysis, DNA quantification and degradation assays. In conclusion, our results evidenced that IPFP-MSCs-loaded b-TPUe scaffolds had higher similarity with cartilage mechanics and T1.5 was the best adapted morphology for CTE.

1. Introduction

Tissue engineering (TE) is a multidisciplinary research area focused on assembling functional constructs that restore, maintain, or improve damaged tissues or whole organs [1]. TE is based on three essential pillars: cells, biomaterials, and external stimuli. In this context, 3D bioprinting is a manufacturing methodology that makes use of biomaterials, cells, proteins, DNA, drugs, and growth factors to ease the restoration and regeneration of injured organs. Among the wide diversity of 3D bioprinting strategies, droplet-based bioprinting (DBB), extrusion-based bioprinting (EBB) and laser-based bioprinting (LBB) are the most commonly used [2]. Each one has its strengths and: as high cost, accuracy, or time-consuming. Perhaps, the main difference between the standard 3D bioprinting manufacturing methods is the

* Correspondence to: J. de Vicente, Department of Applied Physics, Faculty of Sciences, University of Granada, Granada, Spain.
** Correspondence to: J.A. Marchal, Instituto de Investigación Biosanitaria de Granada (ibs.GRANADA), University Hospitals of Granada-University of Granada, Granada, Spain.
E-mail addresses: jvicente@ugr.es (J. de Vicente), jmarchal@ugr.es (J.A. Marchal).

https://doi.org/10.1016/j.msec.2021.111933
Received 21 October 2020; Received in revised form 26 January 2021; Accepted 28 January 2021
Available online 3 February 2021

capability to accurately control the microstructure geometry. In tailor of fibers, it is essential not only to take into account their chemical composition; but also their spatial arrangement because the spatial distribution directly modifies the biomechanical behavior of the construct [3]. Interestingly, the way by which cells interact with the material also depends on the fiber distribution. Thus, the control of the pore interconnectivity, size, and scaffold geometry is a key point to achieve a suitable cell maturation and extracellular matrix formation to have success in 3D bioprinting-based tissue engineering purposes [4]. Even more, tailoring porosity (e.g. pore size, geometry, and orientation), the interconnectivity of the whole scaffold is controlled and together the surface chemistry both are parameters that determine the behavior of nutrient flow [5]. EBB is possibly the easiest way to parametrize the fiber orientation thanks to the possibility to customize the layer degree laydown pattern. More precisely, changing fiber orientation during printing will largely modify the final arrangement of the microstructure without modifying the chemical structure of the material [5]. On the other hand, traditional methodologies like gas foaming, salt-leaching, or cross-linking provide high porosity but the resulting porous interconnectivity depends on several factors that make mandatory the precise control of porous distribution, size, and geometry [6,7].

One of the most widely used thermoplastic biomaterials for cartilage TE (CTE) is poly(e-caprolactone) (PCL), which contrary to conventional thermoplastic materials that have high melting temperatures (above 200 °C), presents a relatively low glass transition temperature (60 °C) that is attractive in bioresorbable polymers [8]. It is also remarkable its thermal stability since its decomposition temperature is around 350 °C whereas other aliphatic polyesters only have a gap of 20–30 °C from their melting point [9]. Among mechanical aspects, PCL is one the most flexible biomaterials (Young's modulus, E ≈ 16 MPa in the solid-state) and it is relatively easy to work with [10]. Moreover, 1,4-butanediol thermoplastic polyurethane (b-TPUe) is a biomaterial with no preceding studies in TE. In comparison with other TPUs (which are petrochemical-based), b-TPUe uses bio-based chain extenders increasing their biocompatibility and biodegradability, and, at the same time, their thermal and mechanical properties are improved [11,12]. Also, b-TPUe is closer to the viscoelastic properties of the cartilage with a storage modulus (G') of 9.6 MPa and a damping factor (tanδ) of 0.18 [13].

Previous studies reported an array of mechanical and biological analyses of the porous architectures of the scaffolds [14–17]. Most of them conclude that porosity depends on two principal aspects: the tissue composition and the cell used [18–20]; however, no conclusive results were reported about the geometry. The main focus of the present study was to investigate and clarify which geometry and pore size tailor optimally the conditions for cell adhesion and proliferation of infrapatellar fat pad derived mesenchymal stem cells (IPFP-MSCs). IPFP-MSCs have probed their huge chondrogenic potential [21–23], which is the tissue that needs to be replaced. In addition, they do not produce collagen type X (cartilage hypertrophy) when they are exposed to chondrogenic differentiation [24]. Even more, IPFP-MSCs maintain chondrogenic potential larger times than chondrocytes obtained from OA patients [25]. Also comparing IPFP-MSCs with bone-marrow MSCs, they produced higher cartilaginous ECM; and, comparing with synovium-derived stem cells, IPFP-MSCs under hydrostatic pressure [26], or under dynamic compression and a gradient oxygen tension presented higher chondrogenic response [27]. Finally, IPFP-MSCs cultured inside decellularized cartilage grafts also showed cartilage ECM synthesis and the zonal architecture which resembles the native tissue [28].

For this purpose, we used for the first-time b-TPUe as 3D bioprinting material in comparison to PCL. For each biomaterial, three different geometries (triangular, square, and hexagonal) and three ranges of pore size (PS) (1, 1.5, and 2 mm) were used. Patterns were analyzed from the mechanical perspective with compression mechanical tests and μCT technology. Besides, the biological behavior of IPFP-MSCs was evaluated using Alamar blue assay, DNA content, and environmental scanning electron microscopy.

The complex structure of this article relapses in the necessity of mixing several material properties with its cell response. In addition, due to a large number of treated variables and samples, the number of them has reduced thanks to the preliminary studies. Thereby: nine different geometries were proposed for the proliferation assay, each one was analytically studied. After, some of those geometries were discarded to simplify deeper analyses, reducing the sample number. Finally, selected geometries were exposed to mechanical assays, microarchitecture analyses, viability tests, and cell-material interactions inquiries.

2. Materials and methods

2.1. Bioprinter setup

REGEMAT 3D V1 bioprinter (Regemat 3D S.L., Granada, Spain) was used as representative of the EBB technique, and the software REGEMAT 3D DESIGNER was used to build scaffold geometries. PCL was obtained from Esun Industrial Co Ltd. (Shenzhen, China) and b-TPUe from Recreus Inc. (Elda, Spain). Their manufacturer parameters are detailed in Supplementary Table 1.

The layer height (LH = 200 μm), the scaffold diameter (14 mm), and the number of perimeters (2 perimeters of 0.4 mm of thickness) were kept constant. No bottom neither top layers were created to ensure that the cells attach to the filaments. Retract speed was 20 mm/s; perimeter/skirt speed 10 mm/s; infill speed 12 mm/s for PCL and 25 mm/s for b-TPUe. Finally, different PS (1, 1.5, and 2 mm) and printing patterns were arranged to modify the porosity. In Supplementary Table 2, it is represented the main parameters used to obtain the desired geometries: hexagonal (H), square (S), and triangular (T). Melting points corresponded with manufacturers' ones.

2.2. Isolation and culture of IPFP-MSCs

IPFP-MSCs were obtained from patients with osteoarthritic knee during joint replacement surgery. Ethical approval for the study was obtained from the Ethics Committee of the Clinical University Hospital of Málaga, Spain (ethic permission number: 02/022010 Hospital Virgen de la Victoria, Málaga). Informed patient consent was obtained for all samples used in this study. IPFP-MSCs isolation and characterization were performed as previously described [30]. The samples were extracted directly from osteoarthritic patients. The infrapatellar fat pad was mechanically and enzymatically (collagenase type I; Sigma-Aldrich) disaggregated at 37 °C heated ovens where they remained under stirring for 2 h. When cells were isolated, the excess of collagenase was eliminating with washes (10% phosphate-buffered saline (PBS) fetal bovine serum (FBS; Sigma-Aldrich) and 1% antibiotic penicillin/streptomycin (P/S)) and the obtained pellet was resuspended in culture medium (DMEM (Sigma-Aldrich), 20% FBS, 1% P/S) and it was transferred to a cell culture flask (75 cm^2). Afterwards, IPFP-MSCs were incubated at 37 °C and 5% CO_2 with DMEM high glucose (Sigma-Aldrich, St Louis, MO, USA) supplemented with 20% FBS (Lonza, Basel, Denmark) and 1% of penicillin/streptomycin (Sigma-Aldrich, St Louis, MO, USA). At 80% of confluency cells were sub-cultured.

2.3. Cell adhesion and proliferation assays in 3D scaffolds

For cell-seeding experiments, PCL and b-TPUe scaffolds were sterilized as follows: i) first, scaffolds were introduced in glass tubes of 30 mL, rinsed out with 50% ethanol/water solution during 10 min; ii) after, scaffolds were introduced into 70% ethanol/water solution for 24 h. iii) Next day, dried scaffolds were deposited onto Petri dishes and they were washed with phosphate-buffered saline (PBS) (0.01 M). iv) Then, they were irradiated with UV light for 40 min. iv) Immediately after, scaffolds were fitted inside 24 well plates and immersed into DMEM high glucose (Sigma-Aldrich, St Louis, MO, USA) supplemented with 10% FBS

(Lonza, Basel, Denmark) and 1% of penicillin/streptomycin (Sigma-Aldrich, St Louis, MO, USA) overnight. All the previous steps together with the printing protocol were carried out inside a sterile laminar hood.

Subsequently, to compute similar conditions 2×10^5 cells were seeded onto the scaffolds. The data acquisition intervals were done at day 1 (d1), day 7 (d7), day 14 (d14), and day 21 (d21); at those times scaffolds were introduced in a new 24 well plate to avoid data contamination of possible cells that were attached to the well bottom.

The proliferation rate of IPFP-MSCs in 3D constructs was assessed by colorimetric alamarBlue® (*BIO-RAD*) assay. Samples were withdrawn from the incubation media, rinsed with PBS, and immersed in alamarBlue® for 3 h. The alamarBlue® reduction pattern was analyzed using a fluorescence spectrometer (Ex 530–560 nm/Em 590 nm BIOTEK synergy4 HT). After that time, the samples were repositioned in a new 24 well plate with 200 μL of fresh culture media.

2.4. Porosity estimation and surface/volume ratio

The porosity (P) and surface/volume (S/V) ratios were theoretically calculated, under the assumption that the fibers had a cylindrical shape. P was also experimentally determined from the relative density ρ_r as follows: $P = 1 - \rho_r$. The relative density was obtained by dividing the experimental density over the theoretical one. More detailed information is described in the supplementary material and methods section.

2.5. Wettability

The degree of scaffold hydrophobicity is one of the principal biomaterial properties, which determines cell interaction [31]. Wettability was estimated by measuring the contact angle (CA) of a deposited water droplet (100 μL of distilled water) over a planar section of each material. An orthogonal image was captured after 2 s and the contact angle was measured with ImageJ.

2.6. Angle frequency

To compute the number of angles that appeared by superposition of fibers in the different geometries, the angle frequency (AF) $\left(A_F = {}^{n\ Angles}/_{n\ Total\ Angles}\right)$ was calculated. Thus, this ratio implies which geometry had a higher number of angles and how was the difference concerning other conformations.

2.7. Mechanical testing of the scaffolds

Mechanical tests were carried out using two different devices to explore a wide strain range of deformations. To explore the small strain range (below approx. 0.2) a commercial rheometer (MCR302, Anton Paar, SE Germany) was used. To explore the mechanical behavior in a larger strain range (from approx. 1 to 20) a Universal Testing Machine (Shimadzu Autograph AGS-X) was used.

The rheometer was operated with a parallel plate geometry. The experimental protocol consisted of four steps. In the first step, a cylindrical scaffold was placed on top of the bottom plate of the rheometer and the upper one was displaced downwards from the "lift position" to the "initial position" $h_s = H_s$ (≈5 mm). The initial position was always larger than the thickness of the scaffolds tested. During this step, the upper plate never touches the scaffold and therefore, data are not recorded. In the second step, the upper plate was displaced downwards at a constant velocity (10 μm/s) to compress the scaffold. The third step began when the normal force reached a value of $F_N = 40$ N. At this point, the plate undergoes a small amplitude strain oscillation (strain amplitude $\gamma_0 = 10^{-5}$% and excitation frequency $f = 1$ Hz) during 10 s to explore the linear viscoelasticity of the scaffold under shear kinematics. In the fourth step, the upper plate was displaced upwards at a velocity of 10 μm/s. All steps were performed in triplicates at 25 °C. The Young's modulus was calculated from the compression interval - as the slope of the linear portion of the stress-strain curve (i.e. X-Y strain) by linear fitting - while storage and loss moduli were obtained from the shear interval -in the viscoelastic linear region (strain < 0.01).

A Universal Testing Machine was used to explore the mechanical properties of the scaffolds in the large strain regime. For this aim, scaffolds with a cubic shape were fabricated and tested in compression along two different axes: the Axial 'out of plane' direction (i.e. orthogonal to the print plate) and the Radial 'in plane' direction (i.e. parallel to the print plate).

2.8. Characterization of the microstructure throughout μCT technology

To analyze the porosity and the microstructure of the scaffolds in deeper detail, μCT was applied in triangular geometries for PS of 1.5 and 2 mm (T1.5 and T2). For each material and PS, three samples were used and analyzed inside an Xradia 510 Verse (Zeiss) for 24 h with an acquisition voltage of 40 kV at 3 W. The emitting distance was 50 mm, whereas the detector distance was 91 mm and the pixel size was 12.1 μm. The magnification objective was 0.4× and the exposure time 18–22 s.

2.9. DNA quantification

The 4′, 6-diamidino-2-phenylindole (DAPI, Sigma-Aldrich, St Louis, MO, USA) assay was used to study the DNA content. Briefly, 50 μL of papain-digested sample harvested from 3D scaffolds at d7, d14, and d21 were added into a 96-well plate and combined with 50 μL of DAPI dye. Afterward, the absorbance at 358 nm was read at 461 nm. To determine the DNA content of the samples, the DNA standard from Calf Thymus (Sigma-Aldrich, St Louis, MO, USA) was used as standard.

2.10. Environmental scanning electron microscope (ESEM)

The scaffolds were imaged with a FEI Quanta 400 microscope (Thermo Fisher Scientific-FEI, Fremont, CA, USA) with an Everhart-Thornley detector (E-TD) for dry and conductive samples in high vacuum mode, and a gaseous SE detector (GSED) for wet samples in the environmental model. Cell-laden PCL and b-TPUe scaffolds with triangular morphology were analyzed at 2 weeks. Afterward, they were fixated with 2% glutaraldehyde for 2 h at room temperature, and then they were rinsed in 0.1 M cacodylate buffer and incubated at 4 °C. The pressure curve adopted for the measurements was 720–1067 Pa.

2.11. Statistical analysis

All graphed data represented the mean ± SD from at least three experiments. All the statistics were performed with n = 3 in OriginLab Pro ™. For mechanical curves and because of simplicity linear interpolation applying average was performed over all samples. To compute statistical significance among geometries, a two-tailed Students t-test was done, and homoscedasticity and normality tests were done before meaning comparison. In graph representations, P-value less than 0.05 was represented $^{*/\#}$; P-value < 0.01 with $^{**/\#\#}$ and P-value < 0.001 $^{***/\#\#\#}$.

3. Results and discussion

3.1. Fabrication approach

Among different options, thermoplastic polymers can be easily printed using the extrusion EBB technology by fused deposition modeling (FDM) consisting of a nozzle with a heater that melts a thermoplastic filament and deposits it in a controlled and organized manner, layer-by-layer, on a surface [32]. The REGEMAT 3D software allows the possibility of tailoring several parameters about the scaffold

arrangement and, in contrast with other EBB-based bioprinters, it does not apply mesh restrictions configuring patterns slightly different from conventional 3D printers as could be the triangular and the hexagonal [33]. In contrast with other common software it takes a 3D volume (in STL format) and from such model makes the lamination [34]. Moreover, this software directly configures the mesh distribution to facilitate the presence of symmetries [33]. In our study, we investigated three different patterns (triangular, square, and hexagonal) and three porosity sizes PS (1, 1.5, and 2 mm). Fig. 1A–C shows the layer arrangement for the three different geometries. The triangular geometry presents a higher number of possible orientations (4), whereas hexagons only present one. Together with the theoretical porosity, the cylindrical approximation allows us to obtain the available surface (i.e. the exposed material surface for cell contact) for the hypothetical volume (see Supplementary Fig. 2) that would take the scaffold in the case of presenting null porosity (see Supplementary Table 3). With all previous considerations, the early defined geometries were fabricated for each biomaterial (Fig. 1D–E). An adequate computer design that controls the thermal conductance and viscosity of the polymer will result in a better fidelity of the final patterns. Comparing Fig. 1D and E, it can be distinguished that b-TPUe presents thinner filaments in comparison with PCL, possibly due to the high thermal conductance of PCL [9]. Another relevant effect that affects the final design is the stability of the pillars that are formed because of the fibers' superposition (see Supplementary Table 2). Thus, it is important to control not only the initial CAD parameters but the printing properties to ensure an optimal scaffold architecture [35].

3.2. Cell adhesion/proliferation assay

In the previous literature, it has been described several factors that increase cell adhesion and proliferation in 3D bioprinted scaffolds [36]. Among others PS, interconnectivity in the scaffold microstructure and surface conformation are key determinants [37–39]. In fact, the exchange of nutrients and cues depends on the porosity and its interconnectivity [16]. Also, surface conformation together with hydrophilicity and PS increases biointegration [40]. Here, the interaction of IPFP-MSCs (see Supplementary Fig. 3 for MSCs characterization) with the two biomaterials (PCL and b-TPUe) was analyzed to characterize their cell adhesion and proliferation profile.

Fig. 2 represents the fold increase proliferation of AlamarBlue® assay for each geometry in both PCL and b-TPUe scaffolds in IPFP-MSCs-loaded scaffolds, proliferation rate decreased from d1 to d7 and increased up to d21 for all geometries. When the fluorescence units were normalized (fold increase) with respect to the values obtained on day 1, it was observed that square and triangular conformations showed similar proliferative levels at day 21, except the hexagonal geometries for PS 1 and 2 mm that showed higher values (Fig. 2A). Fig. 2B and C shows the raw fluorescence units of b-TPUE obtained from the AlamarBlue® reduction assay for d1 and d21 respectively. Four conformations, T1.5, H1.5, S1.5, and S2, displayed higher adhesion at the starting point (Fig. 2B); however, at day 21 all geometries achieved high levels of fluorescence when comparing PS for each geometry, being H2 the one with significantly higher values (Fig. 2C).

On the other hand, Fig. 2D represents the fold increase proliferation curves for PCL. As observed, very different behavior is found when compared with b-TPUe. For all geometries, the proliferative response increases from d1 to d7 and afterward decreases until d21 with ratio values similar to d1. Despite this difference in behavior, there is a shared similarity for PS 2 mm which seems to present a higher proliferative response over the rest of the PS, undependably of spatial conformation. Fig. 2E and F presents the raw data from reduction assays at d1 and d21 for PCL. In both cases, the triangular geometry is associated with the higher levels of metabolism implying much higher adhesion. Similarly, to b-TPU, S2 and H2 also reached very high levels of fluorescence when comparing PS for squares and hexagons, respectively.

Overall, cell adhesion in PCL scaffolds was larger than b-TPUe at d1 (see Fig. 2B and E). A reason for this result is the lower contact angle in PCL (90 $\pm$ 1°) than b-TPUe (111 $\pm$ 2°) that demonstrates a more hydrophilic character of PCL than b-TPUe. These results are in good agreement with previous publications in the literature. In particular, Metwally et al. established that wettability influences cell adhesion and found an inverse correlation between the contact angle and cell proliferation [41].

However, it is remarkable to point that, in contrast to PCL, the proliferation rate is larger for b-TPUe on day 21. These results suggest a better proliferative response for b-TPUe in the long-term in comparison to PCL scaffolds. The higher proliferation response for large PS could be explained because of the higher interconnectivity of the pores allowing a better diffusion of the culture medium [42]. Conclusively, although the cell adhesion results are different depending on the biomaterial; in general, triangular patterns with large PS showed better response. This is remarkable in the case of PCL, making this geometry the most adequate candidate for optimal cell adhesion.

3.3. Correlation of proliferation with experimental porosity and S/V ratio

Based on previous investigations, it can be noticed that the biochemistry and the microstructure of the biomaterial surface affect cell adhesion and proliferation [43]. Also, it is expected that a higher available surface for cell attachment would result in a higher cell adhesion level [44]. Two parameters were used to quantify the amount of surface that is available for cell attachment: the experimental porosity and the surface-to-volume (S/V) ratio. In Supplementary Table 3, results for the theoretical porosity (under the approximation that the fibers can be represented by cylinders) are presented together with the experimental porosity (obtained from ρ_r). As observed, a very good agreement is found between the two values suggesting that: i) the scaffolds almost preserved the original computer design; and, ii) the theoretical model is a good approximation. S/V ratios were also calculated using the cylindrical approximation and included in the Supplementary Table 3. The largest S/V ratio is found for the triangular pattern.

In an attempt to look for correlations between the proliferation rate and the physical characteristics of the scaffolds (porosity and S/V ratio), in Fig. 3 we show the Alamar Blue® reduction fluorescence at days 1, 7, 14, and 21 for all the patterns investigated as a function of the porosity (Fig. 3A) and S/V ratio (Fig. 3B). The fact that the curves are essentially flat in Fig. 3 demonstrates that neither the porosity nor the S/V ratio is the driving factor for cell adhesion and proliferation. Instead, the geometry plays a key role and in particular, triangular patterns are associated with a larger proliferation rate in PCL.

To get a better understanding as to why the triangular pattern is associated with a larger proliferation, in Fig. 3C we show the ratio of the number of angular vertices that exist in a particular scaffold concerning the others. In Fig. 3D it is shown a schematic representation of the geometrical unit cells with their corresponding angles. Given Fig. 3C, the number of angular vertices is larger for those patterns where a larger proliferation is observed. Also important is to note that the connectivity angles in a triangular pattern are also smaller (45° (T) < 90° (T, S) < 120° (H)) hence favoring water entrapment by surface tension [37]. From the observation of Fig. 3C, the higher values for the triangular geometry could explain their good proliferation at day 21 in both materials.

Based on all these results, it can be concluded that the triangular geometry is superior over the rest in terms of cell adhesion and proliferation.

3.4. Mechanical testing

Since these biomaterials and geometrical structures have a potential translation for osteochondral replacements, in this section we analyze both the compression and shear properties of the scaffolds. An adequate mechanical behavior is critical for cellular proliferation as Nam el al.

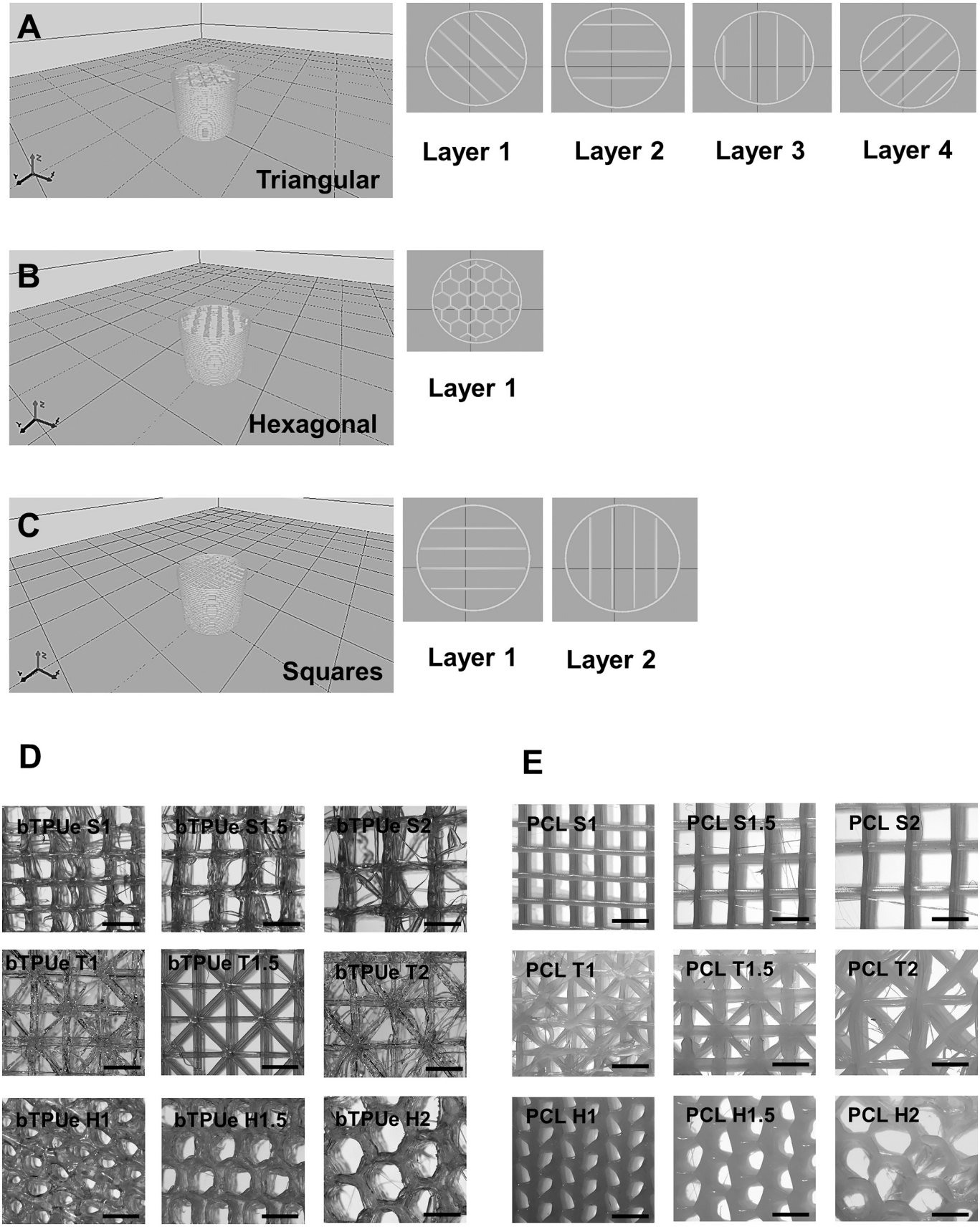

Fig. 1. A–C) STL models of the scaffolds of each layer-down topography (PS 1.5 mm). In A) layers 1,2,3,4 are inserted periodically one on top of the next one. B) The hexagonal pattern only has one layer which is repeated along Z axis. C) In the Square pattern there are two different layers intercalated repeatedly. D–E) Cross-sectional images of the fabricated scaffolds. Scale bars correspond to 2 mm in all cases.

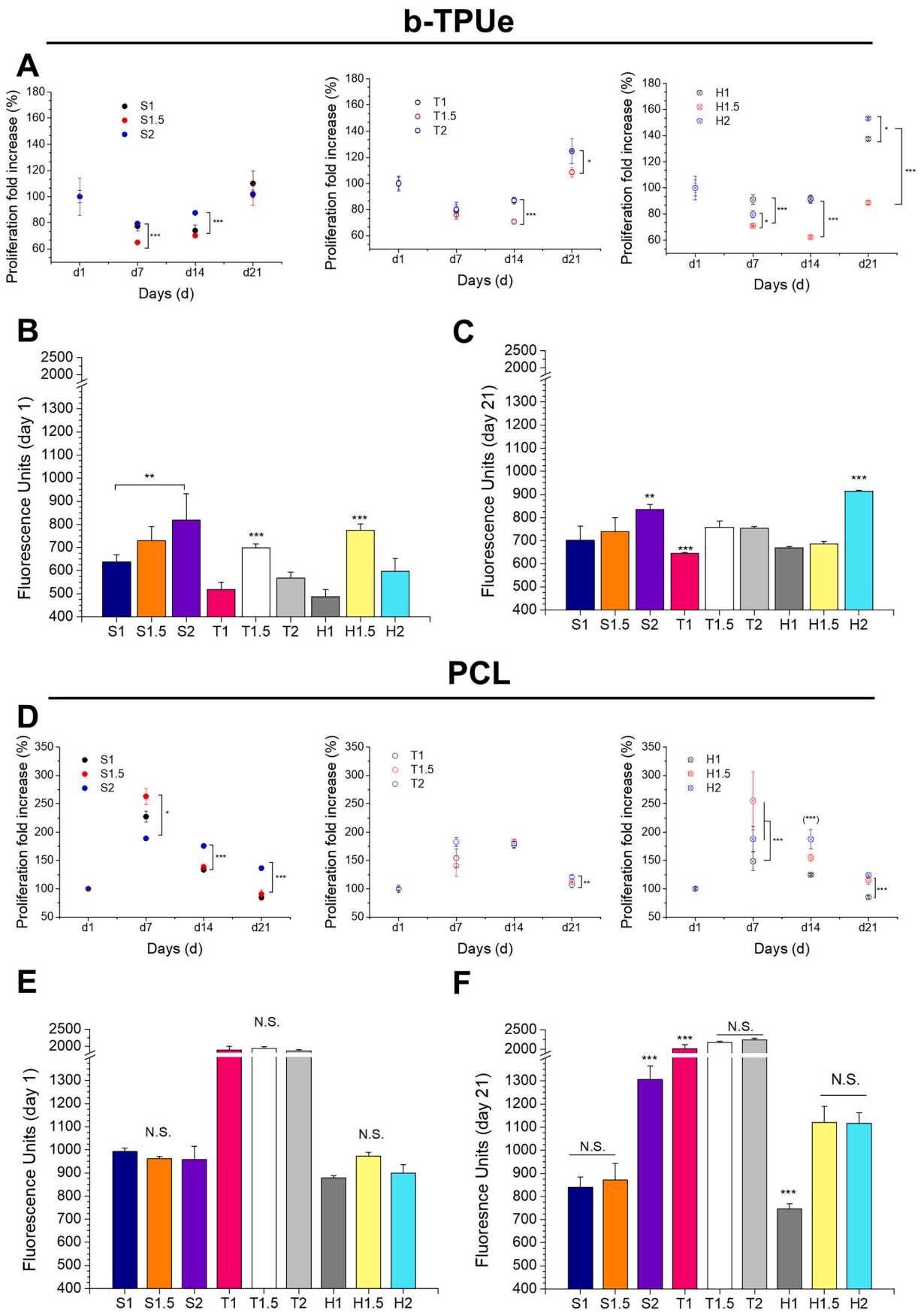

Fig. 2. A & D) Normalized proliferation assays for b-TPUe and PCL materials, respectively. B) Absorbance of fluorescence emitted at 590 nm for b-TPUe at day 1. C) Same as B at day 21. E) Absorbance of fluorescence emitted at 590 nm for PCL at day 1. F) Same as E at day 21. P-value less than 0.05 was represented *; P-value < 0.01 with ** and P-value < 0.001 ***. Brackets mean significance different with the rest of PS inside the same geometry.

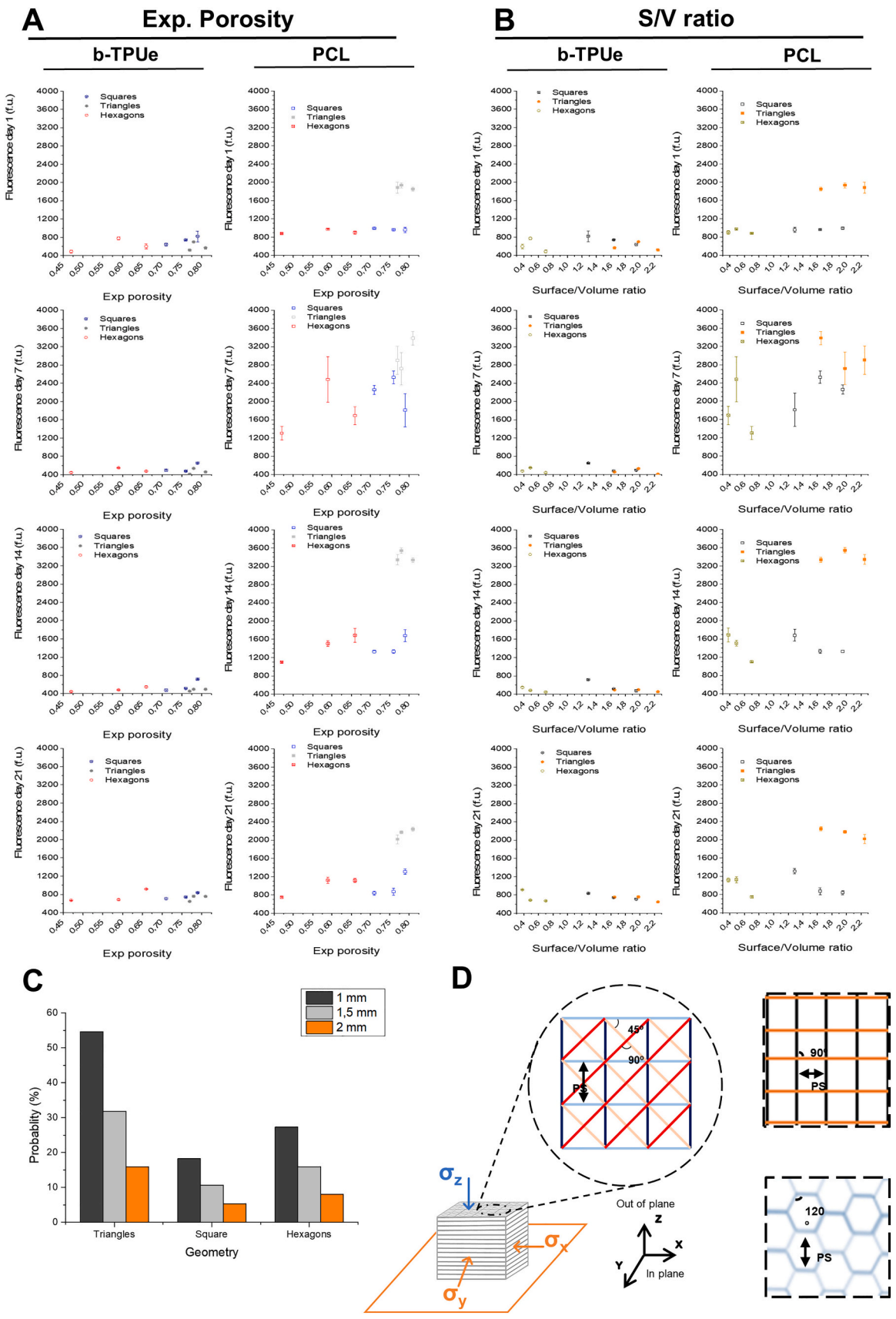

Fig. 3. A) Fluorescence units (590 nm) from AlamarBlue© assay for b-TPUe and PCL scaffolds against their experimental porosity at days 1, 7, 14 and 21 (n = 3). B) Fluorescence units (590 nm) from AlamarBlue© assay for b-TPUe and PCL scaffolds against their S/V ratio at days 1, 7, 14 and 21 (n = 3). C) Angle frequency (AF) for each geometry as obtained from the frequency resulted by dividing the number of angles for each geometry by the total number of angles for all geometries. D) Infographic scheme of how stresses was applied on the scaffolds together with the representation of PS and the different printed angles which affects in cell adhesion.

exposed. They showed how just stiffness changes in the fibers without altering the microstructure inducing the expression of different gene expression [45]. Raw compression curves for the scaffolds are shown in Supplementary Figs. 4–5. These curves are obtained with the rheometer to explore the low strain regime and with the Universal Testing Machine to explore the large strain regime. From these curves, the compression modulus can be obtained by fitting the linear region. Compression modules are summarized in Table 1. As observed, the modulus is strongly dependent on the technique employed in its determination. In particular, the modulus measured with the rheometer is always larger than the one measured with the Universal Testing Machine. Moreover, in consonance with manufacturers' data, b-TPU is clearly softer than PCL and therefore more appropriate for biomedical applications; the modulus of b-TPU is closer to that of cartilage that is around E = 10 kPa. Generally speaking, a decrease in PS is associated with an increase in the stiffness of the scaffolds [14,38]. However, for the scaffolds investigated in this work PS has a minor influence on the compression modulus.

In Fig. 4 we show the stress versus strain curves under compression tests using the Universal Testing Machine. Two important observations are as follows: i) out-of-plane measurements generally give larger moduli than in-plane measurements and ii) specimens with perimeter generally give larger moduli than samples without a perimeter.

The mechanical behavior of the scaffolds under shear is summarized in Table 1. In this table, we show the storage modulus. As observed, a very similar value is obtained independently of the direction (in-plane or out-of-plane), material (PLC or b-TPU), or porosity (PS). The only relevant feature was the presence or absence of a perimeter surrounding the scaffold even though previous works also reported an influence of PS [13]; scaffolds with perimeters exhibited a larger shear modulus.

3.5. Characterization of the microstructure

A deeper study about the microstructure was also performed to understand the precise differences between candidate geometrical morphologies. In 3D bioprinting, there are differences between the computer design and the final printed scaffold. So, μCT technology is an outstanding tool to probe how are the real architecture of the fibers inside the scaffold [46]. Considering previous results, the characterization of the microstructure was done in T1.5 and T2 geometries for both biomaterials. In Fig. 5A to D, there are represented a cross-section corresponding to the middle plane in the axial direction of the scaffolds to analyze not only the fibers' disposition but also the "empty-space" across those fibers [47]. In sagittal sections, it can be appreciated the real distance (in different colors) between the pillars produced by filament conglomeration. Although apparently, there were no significant differences among PCL geometries and b-TPUe; however, a deeper analysis showed that b-TPUe presents lesser distance for both PS which seems to be related to its higher regularity in fiber distribution.

On the other hand, the analysis of the porous interconnectivity (orange ellipses) in the sagittal middle planes, showed that. The accuracy to print perfect cylindrical fibers was almost lost at PS of 2 mm, although for b-TPUe they present higher resolution and homogeneity. Also, there is more homogeneity in the fiber disposition in b-TPUe resulting in continuous lines in the coronal planes (Fig. 5A and C). Those irregularities imply direct consequences because a higher irregularity is proportional to lower space, and higher irregularity implies less isotropy, which derives in pour mechanical toughness [48]. Nonetheless, although the differences between T1.5 and T2 were lower in the b-TPUe; however, these influenced proliferation rates at day 1 as appreciated in Fig. 2D, indicating the necessity of high printing resolution to enhance cell viability and ECM synthesis [49,50].

Further, the analysis of the estimated porosity with image segmentation confirmed our previous results, showing that PS 2 mm had higher porosity than PS 1 mm and that b-TPUe has a higher porosity than PCL at the same PS (Fig. 5E).

Table 1
Mechanical properties of the optimal scaffolds (i.e. triangular patterns with PS 1.5 and 2 mm) in the in-plane/out-of-plane. E_{rheo} corresponds to the Young's modulus as obtained from the rheometer in the 2nd step of the measuring protocol. E_{UTM} corresponds to the Young's modulus as obtained from the Universal Testing Machine. G_{rheo} corresponds to the Shear (storage) modulus as obtained from the rheometer in the 3rd step of the measuring protocol.

	PCL		b-TPU	
	1.5	2	1.5	2
With perimeter				
E_{rheo}*	6400 ± 900/ 1500 ± 700 kPa	2200 ± 100/ 8040 ± 40 kPa	350 ± 10/970 ± 90 kPa	1000 ± 70/ 1400 ± 200 kPa
E_{UTM}**	47 ± 8/140 ± 20 MPa	250 ± 40/150 ± 10 MPa	0.32 ± 0.02/ 11 ± 2 MPa	0.36 ± 0.05/ 10 ± 0.5 MPa
G_{rheo}***	4.2 ± 0.5/3.9 ± 0.2 MPa	4.2 ± 0.5/4.3 ± 0.3 MPa	4.5 ± 0.4/0.4 ± 0.1 MPa	3.1 ± 0.6/2 ± 1 MPa
Without perimeter				
E_{rheo}*	1.1 ± 0.1/0.6 ± 0.5 MPa	0.099 ± 0.003/ 0.6 ± 0.1 MPa	0.14 ± 0.04/ 0.67 ± 0.04 MPa	0.04 ± 0.01/ 0.11 ± 0.02 MPa
E_{UTM}**	1.0 ± 0.3/2.0 ± 0.4 MPa	1.10 ± 0.06/ 1.2 ± 0.3 MPa	2.0 ± 0.6/0.3 ± 0.1 MPa	1.7 ± 0.6/1.5 ± 0.3 MPa
G_{rheo}***	3 ± 2/0.4 ± 0.3 MPa	1.0 ± 0.9/5 ± 1 MPa	0.07 ± 0.03/ 0.3 ± 0.05 MPa	1.0 ± 0.9/1.3 ± 1 MPa

* rheometer Young's modulus
** UTM Young's modulus
*** rheometer relative shear modulus

3.6. DNA quantification

Once it was established that triangular geometries with PS 1.5 and 2 mm combined good optimal mechanical properties and a good proliferative response, cell analysis was continued to elucidate the most suitable combination of geometry and PS for IPFP-MSCs. For this purpose, DNA quantification was used since it is a more rigorous technique for the measurement of the real amount of viable cells inside the 3D scaffolds [51].

The DNA content for each geometry at d7, d14, and d21 was determined (Fig. 5F). Interestingly, on day 7 the DNA content was higher in b-TPUe in contrast with the proliferation curves, and in T1.5 for PCL the DNA content was significantly lesser than the rest of the samples. These results suggest that at early stages there were more cells attached to b-TPUe but with a lower metabolism, indicating a possible poor cell-biomaterial interaction [52]. Moreover, DNA increased in a time-dependent manner up to day 21 for both biomaterials in T1.5 and decreased for T2. These results agree with those obtained in the microstructure study since the real pillar distance was lowest for triangular geometry and lesser PS in each material. Thereby, from the DNA quantification assay, it can be extracted that this final configuration, b-TPUe T1.5, is the one with a better viability response. A main requisite for regenerative medicine applications in the maintenance of cell viability of biofabricated scaffolds over time [53]. Perhaps, it is very important to consider how small variants in mechanics also directly affect cell viability [50,54]. In agreement, our results probed that both geometry and porosity modify mechanics and the microstructure and how both parameters influence cell proliferation and viability. Moreover, we demonstrated that IPFP-MSCs-loaded b-TPUe scaffolds are suitable to maintain growth and viability up to day 21, which makes it a good candidate for cartilage tissue engineering as previously has been proved for other polyurethane scaffolds with regenerative properties [49].

3.7. Study of interactions between cells and biomaterials by ESEM

All previous results evidenced that cell viability and proliferation were better at d21 for T1.5 b-TPUe and T2 PCL. Then, the interactions

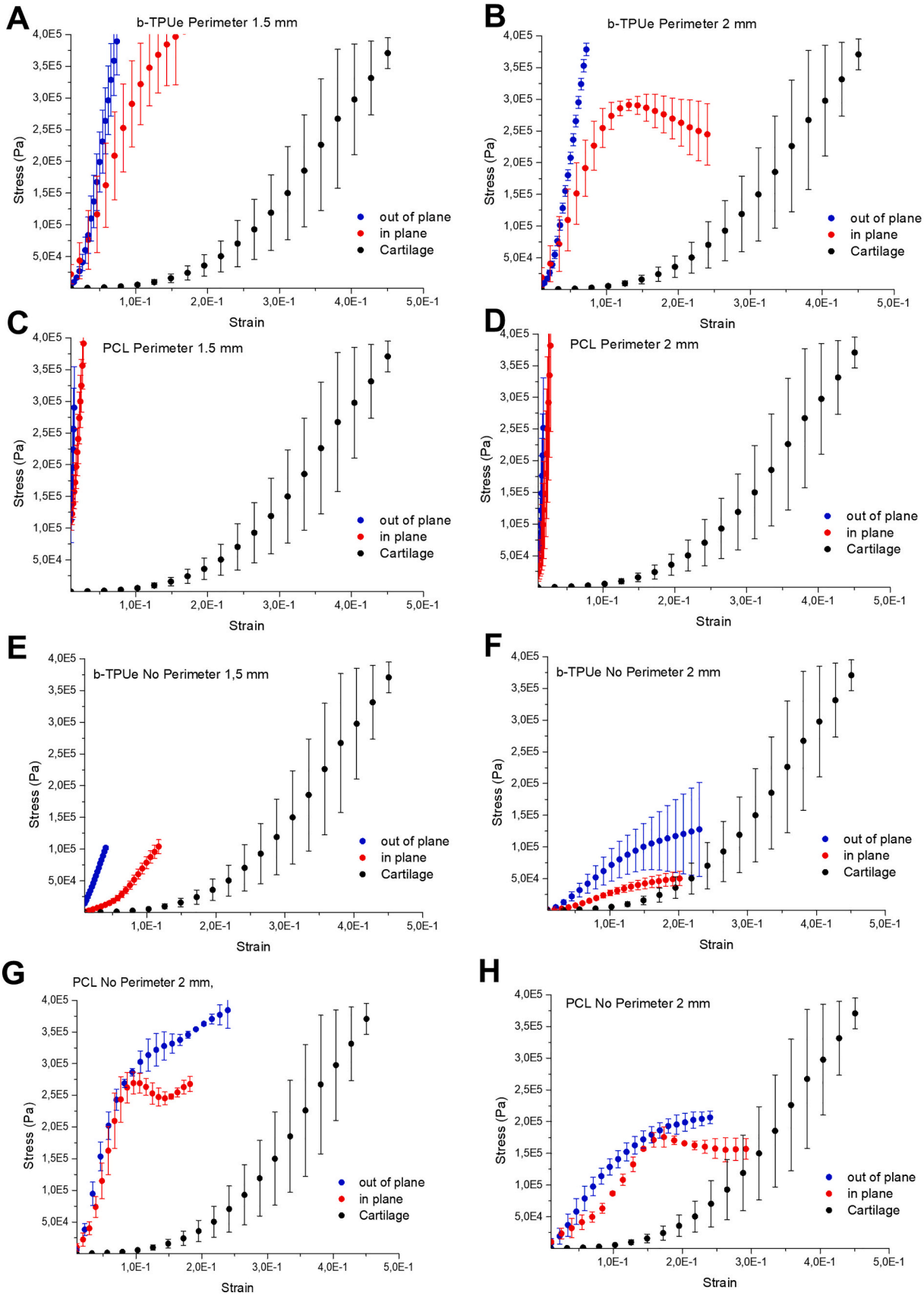

Fig. 4. A–H) Stress-strain curves for the optimal architectures in comparison with the average curve from Cartilage samples. A–D) Samples with perimeters. E–H) Samples without perimeters. Each curve corresponds to the average curve applying linear interpolation (n = 3).

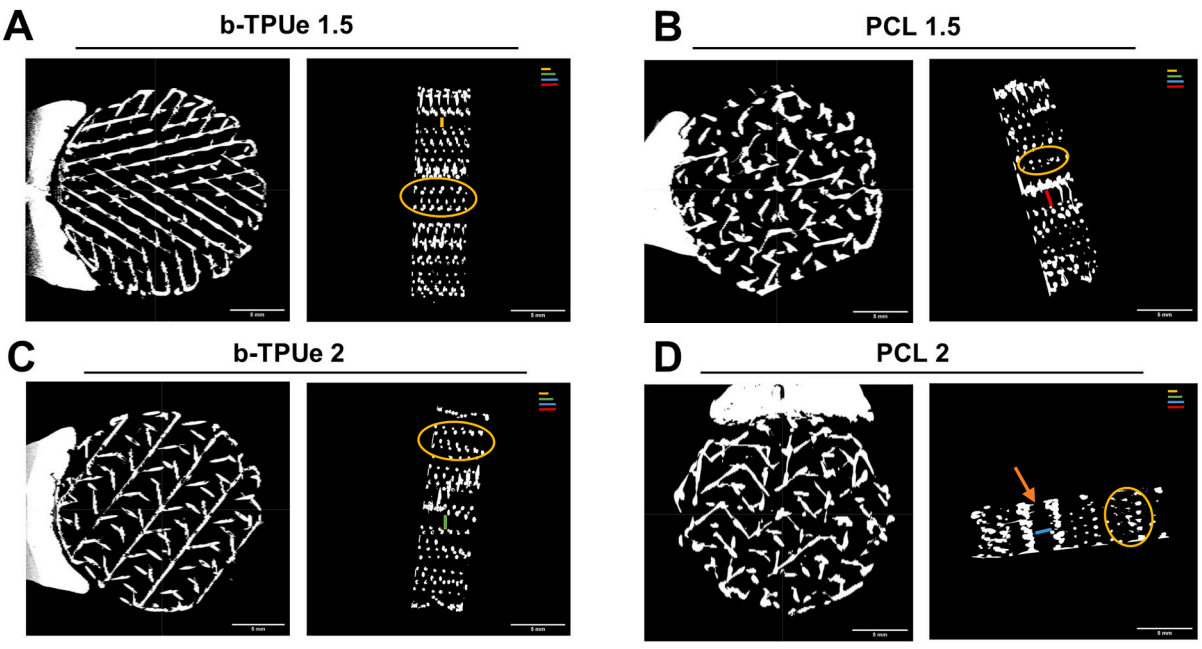

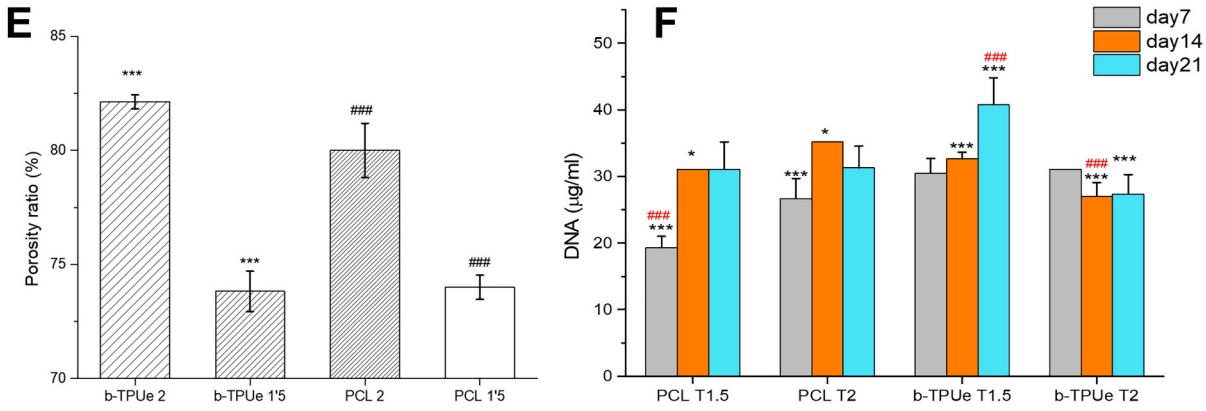

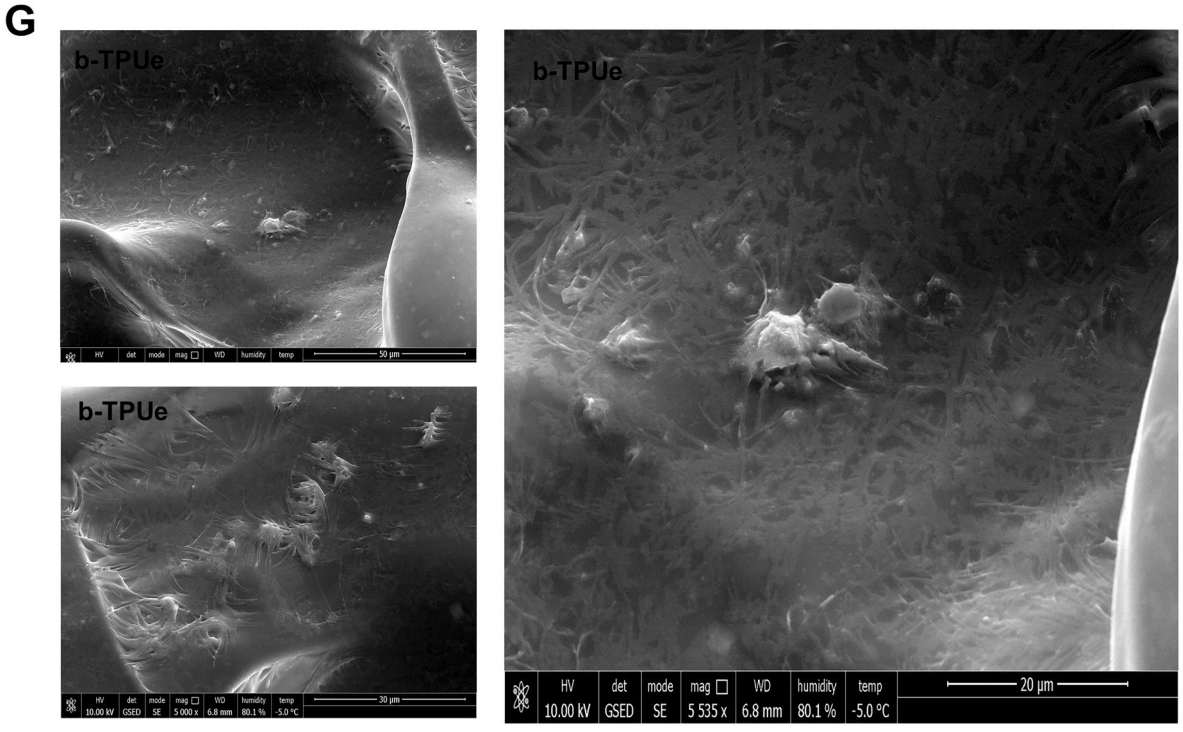

(caption on next page)

Fig. 5. A–D) μCT cross-sectional images (coronal and sagittal middle planes) of T1.5 and T2 geometries. Inside orange circles are presented the 'pillars' formed because of filament superposition among layers. Color bars represents the real distance among those 'pillars' (which should be PS), in the legend they are aligned for comparing sizes between samples. Orange bar corresponds to T1.5 b-TPUe, red bar T1.5 PCL, green bar T2 b-TPUe and blue bar T2 PCL. E) Porosity ratio obtained from segmentation image analysis from μCT technique for b-TPUe and PCL, geometries: T1.5 and T2. P-value less than 0.001 was represented with *** for b-TPUe and with ### for PCL. (n = 3) F) DNA content for PCL and b-TPUe in T1.5 and T2 geometries. P-value less than 0.05 was represented *; P-value < 0.01 with ** and P-value < 0.001 *** among equal material. P-value < 0.001 ### with respect the rest of cases. G) ESEM images of b-TPUe T1. In the amplified picture, it is localized what seems ECM from ifpMSCs. b-TPUe seems to present some rugosity at microstructure, and, consequently there are found more cells attached. (For interpretation of the references to color in this figure legend, the reader is referred to the web version of this article.)

between IPFP-MSCs and both biomaterials by ESEM were analyzed, a technique that enables the investigation of both cell and material surface morphology in hydrated conditions [55]. ESEM images on day 21 revealed that IPFP-MSCs attached to the T1.5 b-TPUe scaffolds (Fig. 5G) actively produced a dense ECM that covered the surface and enhanced their integration with the material. On the other hand, T2 PCL showed less ECM production and areas with lesser cells attached to the biomaterial surface (Supplementary Fig. 6).

In future work, it will be interesting to assess whether changes in pore size or geometry will increase or decrease the chondrogenic potency of the scaffold. Heang Oh et al. demonstrated a slight influence of the diameter of cylindrical pores [56]. However, a lack of cartilage control of induced chondrogenic MSCs, prevents an accurate comparison to extrapolate a real effect on how geometry influences chondrogenesis. Contrarily, Singh et al. showed the importance of scaffold stiffness for chondrogenesis [57] and evidenced that growth factors (like TGF-β3) induce deeply this process. Thus, although geometry can optimize the cell niche and ECM production; a combination of tailored scaffold biomechanics, with specific growth factors, should be recommended for cartilage tissue engineering. However, it would be interesting to analyze the possible effects of geometry in the chemical cues' doses. Despite this, such analyses are out of the scope of this research.

4. Conclusions

In this work, an extensive study was completed using two different biomaterials (b-TPU and PCL) oriented to CTE applications. We demonstrated how the pore geometry and PS of biofabricated IPFP-MSCs-loaded scaffolds affected the final cell viability and adhesion. To fulfill this purpose EBB was done with both biomaterials tailoring different aspects of their microstructure to quantify the relationships between porosity, design, and their mechanical properties. We confirmed that geometry is a key parameter for cellular interaction with the biomaterial, not only because of PS but also by fiber orientation as suggested by our analysis from S/V ratio and AF. Thus, it was demonstrated that at higher interconnectivity of fibers and, as a consequence of higher exposed angle frequency, presents higher biointegration. It was shown that decreasing the PS increased the stiffness of the scaffold independently of the biomaterial. Besides, it is the first time that the huge importance of the perimeter in scaffolds rigidity was clearly exposed, making this aspect of scaffold architecture a key factor for good cell integration and biomechanical properties. A deeper analysis playing with the perimeter of cribbed architectures (T1.5 and T2) was inspected making the T1.5 b-TPUe the optimum geometry and biomaterial for IPFP-MSCs. In summary, our data suggest the necessity of designing the pore geometry and the scaffold microstructure to optimize the better 3D constructs for applications on CTE. This will improve the reliability of a good biointegration of 3D constructs in regenerative medicine of cartilage injures.

CRediT authorship contribution statement

JAM and JdeV conceived the study, designed the experiments, prepared the manuscript, and got the funding. DMM and CCW designed and printed the scaffolds and cellular extraction protocol. EC and EM collected and processed patient samples. GJ, JdeV, PGM, and JAM revised critically the manuscript for important intellectual content. GJ and DMM carried out the proliferation and viability assays. DMM and JdeV did mechanical testing. DMM did the mathematical analysis, approximation, and microCT analysis. DMM, GJ, BCN, CGL, GR, PGM carried out data collection and analysis. DMM, GJ, JdeV, and JAM designed the study and wrote the manuscript. All authors read and approved the final version of the manuscript.

Declaration of competing interest

The authors declare that they have no known competing financial interests or personal relationships that could have appeared to influence the work reported in this paper.

Acknowledgments

This work was supported by the Ministerio de Economía, Industria y Competitividad (ERDF funds, project RTC-2016-5451-1), by the Ministerio de Ciencia, Innovación y Universidades (ERDF funds and project PID2019-104883GB-I00), by Fundación Mutua Madrileña (project FMM-AP17196-2019), by the Consejería de Economía, Conocimiento, Empresas y Universidad de la Junta de Andalucía (ERDF funds, projects B-CTS-230-UGR18, PY18-2470, SOMM17-6109 and P18-FR-2465) and the Instituto de Salud Carlos III, ERDF funds (DTS19/00145). Ministry of Education, Culture and Sports grants DPI2017-83859-R, EQC2018-366 004508-P and UNGR15-CE-3664; Ministry of Health, Social Services and Equality grant DTS15/00093; and Junta de Andalucía grants B-TEP-026-UGR18, IE2017-5537, P18-RT-1653.

Appendix A. Supplementary data

Supplementary data to this article can be found online at https://doi.org/10.1016/j.msec.2021.111933.

References

[1] R. Langer, J.P. Vacanti, C.A. Vacanti, A. Atala, L.E. Freed, G. Vunjak-Novakovic, Tissue Engineering: Biomedical Applications, Tissue Eng. 1 (1995) 151–161, https://doi.org/10.1089/ten.1995.1.151.
[2] I.T. Ozbolat, Introduction, 3D Bioprint. (2017) 1–12, https://doi.org/10.1016/B978-0-12-803010-3.00001-9.
[3] C.G. Jeong, H. Zhang, S.J. Hollister, Three-dimensional poly(1,8-octanediol-co-citrate) scaffold pore shape and permeability effects on sub-cutaneous in vivo chondrogenesis using primary chondrocytes, Acta Biomater. 7 (2011) 505–514, https://doi.org/10.1016/j.actbio.2010.08.027.
[4] B.S. Chang, C.K. Lee, K.S. Hong, H.J. Youn, H.S. Ryu, S.S. Chung, K.W. Park, Osteoconduction at porous hydroxyapatite with various pore configurations, Biomaterials (2000), https://doi.org/10.1016/S0142-9612(00)00030-2.
[5] I.T. Ozbolat, B. Koc, 3D hybrid wound devices for spatiotemporally controlled release kinetics., Comput, Methods Programs Biomed. 108 (2012) 922–931, https://doi.org/10.1016/j.cmpb.2012.05.004.
[6] J. Zhang, L. Wu, D. Jing, J. Ding, A comparative study of porous scaffolds with cubic and spherical macropores, Polymer (Guildf) (2005), https://doi.org/10.1016/j.polymer.2005.02.120.
[7] V. Karageorgiou, D. Kaplan, Porosity of 3D biomaterial scaffolds and osteogenesis, Biomaterials (2005), https://doi.org/10.1016/j.biomaterials.2005.02.002.
[8] A. Vieira, R. Guedes, V. Tita, Considerations for the design of polymeric biodegradable products, J. Polym. Eng. 33 (2013) 293–302, https://doi.org/10.1515/polyeng-2012-0150.
[9] L.J. Suggs, S.A. Moore, A.G. Mikos, Synthetic biodegradable polymers for medical applications, in: Phys. Prop. Polym. Handb., Springer, 2007, pp. 939–950.
[10] I. Engelberg, J. Kohn, Physico-mechanical properties of degradable polymers used in medical applications: a comparative study, Biomaterials, 1991. https://doi.org/10.1016/0142-9612(91)90037-B.
[11] J. Datta, P. Kasprzyk, K. Błażek, M. Włoch, Synthesis, structure and properties of poly(ester-urethane)s obtained using bio-based and petrochemical 1,3-propanediol

and 1,4-butanediol, J. Therm. Anal. Calorim. 130 (2017) 261–276. doi:https://doi.org/10.1007/s10973-017-6558-z.
[12] Z. Wang, J. Yan, T. Wang, Y. Zai, L. Qiu, Q. Wang, Fabrication and properties of a bio-based biodegradable thermoplastic polyurethane elastomer, Polymers (Basel). 11 (2019) 1121, https://doi.org/10.3390/polym11071121.
[13] L. Moroni, J.R. De Wijn, C.A. Van Blitterswijk, 3D fiber-deposited scaffolds for tissue engineering: influence of pores geometry and architecture on dynamic mechanical properties, Biomaterials. 27 (2006) 974–985. doi:https://doi.org/10.1016/j.biomaterials.2005.07.023.
[14] M. Domingos, F. Intranuovo, T. Russo, R. De Santis, A. Gloria, L. Ambrosio, J. Ciurana, P. Bartolo, The first systematic analysis of 3D rapid prototyped poly (ε-caprolactone) scaffolds manufactured through BioCell printing: the effect of pore size and geometry on compressive mechanical behaviour and in vitro hMSC viability, Biofabrication. 5 (2013), https://doi.org/10.1088/1758-5082/5/4/045004.
[15] Z.Z. Zhang, D. Jiang, J.X. Ding, S.J. Wang, L. Zhang, J.Y. Zhang, Y.S. Qi, X.S. Chen, J.K. Yu, Role of scaffold mean pore size in meniscus regeneration, Acta Biomater. 43 (2016) 314–326, https://doi.org/10.1016/j.actbio.2016.07.050.
[16] J. Zeltinger, J.K. Sherwood, D.A. Graham, R. Müeller, L.G. Griffith, Effect of pore size and void fraction on cellular adhesion, proliferation, and matrix deposition, Tissue Eng. (2001), https://doi.org/10.1089/107632701753213183.
[17] A.D. Olubamiji, Z. Izadifar, J.L. Si, D.M.L. Cooper, B.F. Eames, D.X.B. Chen, Modulating mechanical behaviour of 3D-printed cartilage-mimetic PCL scaffolds: influence of molecular weight and pore geometry, Biofabrication. 8 (2016), https://doi.org/10.1088/1758-5090/8/2/025020.
[18] J.W. Lee, G. Ahn, D.W. Cho, J.Y. Kim, Evaluating cell proliferation based on internal pore size and 3D scaffold architecture fabricated using solid freeform fabrication technology, J. Mater. Sci. Mater. Med. (2010), https://doi.org/10.1007/s10856-010-4173-7.
[19] J.P. Temple, D.L. Hutton, B.P. Hung, P.Y. Huri, C.A. Cook, R. Kondragunta, X. Jia, W.L. Grayson, Engineering anatomically shaped vascularized bone grafts with hASCs and 3D-printed PCL scaffolds, J. Biomed. Mater. Res. - Part A. 102 (2014) 4317–4325, https://doi.org/10.1002/jbm.a.35107.
[20] S. Park, G. Kim, Y.C. Jeon, Y. Koh, W. Kim, 3D polycaprolactone scaffolds with controlled pore structure using a rapid prototyping system, J. Mater. Sci. Mater. Med. 20 (2009) 229–234, https://doi.org/10.1007/s10856-008-3573-4.
[21] H. V Almeida, G.M. Cunniffe, T. Vinardell, C.T. Buckley, F.J. O'Brien, D.J. Kelly, Coupling freshly isolated CD44(+) Infrapatellar fat pad-derived stromal cells with a TGF-β3 eluting cartilage ECM-derived scaffold as a single-stage strategy for promoting chondrogenesis., Adv. Healthc. Mater. 4 (2015) 1043–1053. doi:https://doi.org/10.1002/adhm.201400687.
[22] G. Jiménez, S. Venkateswaran, E. López-Ruiz, M. Perán, S. Pernagallo, J.J. Díaz-Monchón, R.F. Canadas, C. Antich, J.M. Oliveira, A. Callanan, R. Walllace, R. L. Reis, E. Montañez, E. Carrillo, M. Bradley, J.A. Marchal, A soft 3D polyacrylate hydrogel recapitulates the cartilage niche and allows growth-factor free tissue engineering of human articular cartilage, Acta Biomater. 90 (2019) 146–156, https://doi.org/10.1016/j.actbio.2019.03.040.
[23] E. López-Ruiz, M. Perán, J. Cobo-Molinos, G. Jiménez, M. Picón, M. Bustamante, F. Arrebola, M.C. Hernández-Lamas, A.D. Delgado-Martínez, E. Montañez, J. A. Marchal, Chondrocytes extract from patients with osteoarthritis induces chondrogenesis in infrapatellar fat pad-derived stem cells., Osteoarthr, Cartil. 21 (2013) 246–258, https://doi.org/10.1016/j.joca.2012.10.007.
[24] M.Q. Wickham, G.R. Erickson, J.M. Gimble, T.P. Vail, F. Guilak, Multipotent stromal cells derived from the infrapatellar fat pad of the knee, Clin, Orthop. Relat. Res. (2003), https://doi.org/10.1097/01.blo.0000072467.53786.ca.
[25] A. English, E.A. Jones, D. Corscadden, K. Henshaw, T. Chapman, P. Emery, D. McGonagle, A comparative assessment of cartilage and joint fat pad as a potential source of cells for autologous therapy development in knee osteoarthritis, Rheumatology (2007), https://doi.org/10.1093/rheumatology/kem217.
[26] S.F. Carroll, C.T. Buckley, D.J. Kelly, Cyclic hydrostatic pressure promotes a stable cartilage phenotype and enhances the functional development of cartilaginous grafts engineered using multipotent stromal cells isolated from bone marrow and infrapatellar fat pad, J. Biomech. (2014), https://doi.org/10.1016/j.jbiomech.2013.12.006.
[27] L. Luo, A.R. O'Reilly, S.D. Thorpe, C.T. Buckley, D.J. Kelly, Engineering zonal cartilaginous tissue by modulating oxygen levels and mechanical cues through the depth of infrapatellar fat pad stem cell laden hydrogels, J. Tissue Eng. Regen. Med. (2017). doi:https://doi.org/10.1002/term.2162.
[28] L. Luo, J.Y.J. Chu, R. Eswaramoorthy, K.J. Mulhall, D.J. Kelly, Engineering tissues that mimic the zonal nature of articular cartilage using decellularized cartilage explants seeded with adult stem cells, ACS Biomater. Sci. Eng. (2017), https://doi.org/10.1021/acsbiomaterials.6b00020.
[30] E. López-Ruiz, G. Jiménez, W. Kwiatkowski, E. Montañez, F. Arrebola, E. Carrillo, S. Choe, J.A. Marchal, M. Perán, Impact of TGF-β family-related growth factors on chondrogenic differentiation of adipose-derived stem cells isolated from lipoaspirates and infrapatellar fat pads of osteoarthritic patients, Eur. Cells Mater. (2018), https://doi.org/10.22203/eCM.v035a15.
[31] H.Y. Mi, X. Jing, M.R. Salick, T.M. Cordie, X.F. Peng, L.S. Turng, Properties and fibroblast cellular response of soft and hard thermoplastic polyurethane electrospun nanofibrous scaffolds, J. Biomed. Mater. Res. - Part B Appl. Biomater. 103 (2015) 960–970, https://doi.org/10.1002/jbm.b.33271.
[32] C.M. O'Brien, B. Holmes, S. Faucett, L.G. Zhang, Three-dimensional printing of nanomaterial scaffolds for complex tissue regeneration, Tissue Eng. B Rev. (2015), https://doi.org/10.1089/ten.teb.2014.0168.
[33] J.M. Baena, G. Jiménez, E. López-Ruiz, C. Antich, C. Griñán-Lisón, M. Perán, P. Gálvez-Martín, J.A. Marchal, Volume-by-volume bioprinting of chondrocytes-alginate bioinks in high temperature thermoplastic scaffolds for cartilage regeneration, Exp, Biol. Med. (2019), https://doi.org/10.1177/1535370218821128.
[34] A.R.G. Cortes, K. Galea, J. No-Cortes, E.J. Sammut, E.E. Alzoubi, N.J. Attard, Use of free CAD design software for 3D printing individualized face masks based on face scans, Int. J. Comput. Dent. (2020) 1–7.
[35] M. Rabionet, E. Polonio, A. Guerra, J. Martin, T. Puig, J. Ciurana, Design of a scaffold parameter selection system with additive manufacturing for a biomedical cell culture, Materials (Basel). 11 (2018) 1427, https://doi.org/10.3390/ma11081427.
[36] Q. Ran, W. Yang, Y. Hu, X. Shen, Y. Yu, Y. Xiang, K. Cai, Osteogenesis of 3D printed porous Ti6Al4V implants with different pore sizes, J. Mech. Behav. Biomed. Mater. (2018), https://doi.org/10.1016/j.jmbbm.2018.04.010.
[37] M. Tanaka, A. Takayama, E. Ito, H. Sunami, S. Yamamoto, M. Shimomura, Effect of pore size of self-organized honeycomb-patterned polymer films on spreading, focal adhesion, proliferation, and function of endothelial cells, J. Nanosci. Nanotechnol. (2007), https://doi.org/10.1166/jnn.2007.514.
[38] H. Wang, J. Pieper, F. Péters, C.A. Van Blitterswijk, E.N. Lamme, Synthetic scaffold morphology controls human dermal connective tissue formation, J. Biomed. Mater. Res. - Part A. (2005), https://doi.org/10.1002/jbm.a.30232.
[39] S. Yang, K.F. Leong, Z. Du, C.K. Chua, The design of scaffolds for use in tissue engineering, Part I. Traditional factors, Tissue Eng. (2001), https://doi.org/10.1089/107632701753337645.
[40] Z. Cheng, S.H. Teoh, Surface modification of ultra thin poly (ε-caprolactone) films using acrylic acid and collagen, Biomaterials (2004), https://doi.org/10.1016/j.biomaterials.2003.08.038.
[41] S. Metwally, U. Stachewicz, Surface potential and charges impact on cell responses on biomaterials interfaces for medical applications, Mater. Sci. Eng. C (2019), https://doi.org/10.1016/j.msec.2019.109883.
[42] B.J. Lawrence, S.V. Madihally, Cell colonization in degradable 3D porous matrices., Cell Adh, Migr. (2008), https://doi.org/10.4161/cam.2.1.5884.
[43] K. Vuoriluoto, J. Jokinen, K. Kallio, M. Salmivirta, J. Heino, J. Ivaska, Syndecan-1 supports integrin α2β1-mediated adhesion to collagen, Exp, Cell Res. 314 (2008) 3369–3381, https://doi.org/10.1016/j.yexcr.2008.07.005.
[44] S.H. Keshel, S.N.K. Azhdadi, A. Asefnejad, M. Sadraeian, M. Montazeri, E. Biazar, The relationship between cellular adhesion and surface roughness for polyurethane modified by microwave plasma radiation, Int. J. Nanomedicine 6 (2011) 641–647, https://doi.org/10.2147/ijn.s17218.
[45] J. Nam, J. Johnson, J.J. Lannutti, S. Agarwal, Modulation of embryonic mesenchymal progenitor cell differentiation via control over pure mechanical modulus in electrospun nanofibers, Acta Biomater. 7 (2011) 1516–1524, https://doi.org/10.1016/j.actbio.2010.11.022.
[46] I.F. Cengiz, J.M. Oliveira, R.L. Reis, Micro-CT – a digital 3D microstructural voyage into scaffolds: a systematic review of the reported methods and results, Biomater. Res. 22 (2018) 26, https://doi.org/10.1186/s40824-018-0136-8.
[47] A. Gleadall, D. Visscher, J. Yang, D. Thomas, J. Segal, Review of additive manufactured tissue engineering scaffolds: relationship between geometry and performance, Burn, Trauma. 6 (2018) 19, https://doi.org/10.1186/s41038-018-0121-4.
[48] J.G. Skedros, S.M. Sorenson, Y. Takano, C.H. Turner, Dissociation of mineral and collagen orientations may differentially adapt compact bone for regional loading environments: results from acoustic velocity measurements in deer calcanei, Bone. 39 (2006) 143–151, https://doi.org/10.1016/j.bone.2005.12.007.
[49] T. Jensen, H. Wanczyk, I. Sharma, A. Mitchell, W.N. Sayej, C. Finck, Polyurethane scaffolds seeded with autologous cells can regenerate long esophageal gaps: an esophageal atresia treatment model, J. Pediatr. Surg. 54 (2019) 1744–1754, https://doi.org/10.1016/j.jpedsurg.2018.09.024.
[50] J. Zhang, E. Wehrle, J.R. Vetsch, G.R. Paul, M. Rubert, R. Müller, Alginate dependent changes of physical properties in 3D bioprinted cell-laden porous scaffolds affect cell viability and cell morphology., Biomed. Mater. 14 (2019) 65009. doi:https://doi.org/10.1088/1748-605X/ab3c74.
[51] V.M.C. Quent, D. Loessner, T. Friis, J.C. Reichert, D.W. Hutmacher, Discrepancies between metabolic activity and DNA content as tool to assess cell proliferation in cancer research, J. Cell. Mol. Med. (2010), https://doi.org/10.1111/j.1582-4934.2010.01013.x.
[52] S.E. Winograd-Katz, R. Fässler, B. Geiger, K.R. Legate, The integrin adhesome: from genes and proteins to human disease, Nat. Rev. Mol. Cell Biol. 15 (2014) 273–288, https://doi.org/10.1038/nrm3769.
[53] R. Levato, W.R. Webb, I.A. Otto, A. Mensinga, Y. Zhang, M. van Rijen, R. van Weeren, I.M. Khan, J. Malda, The bio in the ink: cartilage regeneration with bioprintable hydrogels and articular cartilage-derived progenitor cells, Acta Biomater. (2017), https://doi.org/10.1016/j.actbio.2017.08.005.
[54] Y. Yan, Y. Li, L. Song, C. Zeng, Y. Li, Pluripotent stem cell expansion and neural differentiation in 3-D scaffolds of tunable Poisson's ratio, Acta Biomater. 49 (2017) 192–203, https://doi.org/10.1016/j.actbio.2016.11.025.
[55] M. Parvinzadeh Gashti, J. Hulliger, M. Burgener, H. Oulevey-Aboulfad, F. Alimohammadi, G. Bowlin, Microscopic methods to study the structure of scaffolds in bone tissue engineering: a brief review, in: 2012: pp. 625–638.
[56] S.H. Oh, T.H. Kim, G. Il Im, J.H. Lee, Investigation of pore size effect on chondrogenic differentiation of adipose stem cells using a pore size gradient scaffold, Biomacromolecules. 11 (2010) 1948–1955, https://doi.org/10.1021/bm100199m.
[57] N. Singh, S.S. Rahatekar, K.K.K. Koziol, T.H.S. Ng, A.J. Patil, S. Mann, A. P. Hollander, W. Kafienah, Directing chondrogenesis of stem cells with specific blends of cellulose and silk, Biomacromolecules. 14 (2013) 1287–1298, https://doi.org/10.1021/bm301762p.